

**ELECTROCHEMICAL DETECTION OF NITROFURANTOIN ON  
GRAPHENE NANORIBBONS/MANGANESE DIOXIDE NANOPATES  
MODIFIED ELECTRODE  
DISSERTATION**

*Submitted to the*

**MADRAS CHRISTIAN COLLEGE (AUTONOMOUS)**

*Affiliated to the University of Madras*

*in partial fulfillment of the requirements for the award of the degree of*

**MASTER OF SCIENCE  
IN CHEMISTRY**

*by*

**ACSIA REGI J  
Reg. No: 2001722049001**



**DEPARTMENT OF CHEMISTRY (SFS)  
MADRAS CHRISTIAN COLLEGE (AUTONOMOUS)  
TAMBARAM EAST, CHENNAI – 600 059**

**MAY 2022**

## CERTIFICATE

This is to certify that the dissertation entitled, “**Electrochemical Detection of Nitrofurantoin on Graphene Nanoribbons/Manganese Dioxide Nanoplates Modified Electrode**” submitted by Miss. **ACSIA REGI J** (Reg. No.2001722049001) to the Madras Christian College (Autonomous), Chennai in May 2022, in partial fulfillment of the requirements for the degree of Master of Science, is the original and independent work carried out by her in Saveetha Dental College and Hospitals, Saveetha Institute of Medical and Technical Sciences, Chennai during the period June 2021 to May 2022. This is also to certify that the project work has not been previously formed as the basis for the award of any Degree, Diploma, Associateship, Fellowship, or any other similar titles.

**Dr. K. Vijayalakshmi**

Research Supervisor (Internal),  
Assistant Professor,  
Department of Chemistry (SFS),  
Madras Christian College,  
Tambaram, Chennai - 600 059.

**Dr. Ashok K. Sundramoorthy**

Research Supervisor (External),  
Professor, Material Science,  
Department of Prosthodontics,  
Saveetha Dental College and Hospitals,  
Poonamallee High Road, Velappanchavadi,  
Chennai – 600 077.

**Dr. S. Sahila**

Assistant Professor In-charge,  
Department of Chemistry (SFS),  
Madras Christian College,  
Tambaram, Chennai - 600 059.

## DECLARATION

I hereby declare that the dissertation entitled, “**Electrochemical Detection of Nitrofurantoin on Graphene Nanoribbons/Manganese Dioxide Nanoplates Modified Electrode**” submitted by **ACSIA REGI J (Reg. No. 2001722049001)** to the Madras Christian College(Autonomous), Chennai in May 2022, in partial fulfillment of the requirements for the degree of Master of Science, is the original and independent work carried out by her in the Department of Chemistry, Madras Christian College (Autonomous), Tambaram, under the supervision of **Dr. K. VIJAYALAKSHMI**, Assistant Professor, Department of Chemistry, Madras Christian College and partly in Saveetha Dental College And Hospitals under the supervision of **Dr. ASHOK KUMAR SUNDRAMOORTHY**, Professor, Material Science, Department of Prosthodontics. This dissertation has not previously formed the basis for the award of any Degree, Diploma, Associateship, Fellowship, or other similar titles.

**ACSIA REGI J**

**Reg No: 2001722049001**

## ACKNOWLEDGEMENT

At the outset, I bow my head and offer my thanks to God almighty for the never-failing grace and blessings to complete the project work.

With immense pleasure, I record our gratitude to my external research supervisor **Dr. Ashok K. Sundramoorthy**, Saveetha Dental College and Hospitals, Saveetha Institute of Medical and Technical Sciences, Chennai, for his instituting guidance, continued assistance, inspiration, and involvement throughout my research work.

I am extremely thankful to **Dr. K. Vijayalakshmi**, internal supervisor, Assistant Professor, Department of Chemistry (SFS), Madras Christian College, Chennai, for her encouragement and support in this study.

I express my sincere gratitude to the Principal **Dr. Paul Wilson**, and the SFS Director **Dr. Jannet Vennila** for giving me the opportunity to do the project.

I express my sincere thanks to **Mrs. S. Sahila, Assistant Professor In-Charge** for her continuous support throughout my project work.

I extend my gratitude to **Dr. S. Daniel Abraham** and **Dr. S. Saranya**, Assistant professors, and the Non-Teaching Members of the Department of Chemistry, Madras Christian College (Autonomous) Tambaram East, Chennai, for their enthusiastic encouragement and trust in me during this course.

I sincerely thank Ph.D. Research Scholars of the Department of Prosthodontics, Saveetha Dental College and Hospitals, Saveetha Institute of Medical and Technical Sciences, Chennai for their great support and help during my project work.

I am highly indebted to my project supervisor and all research scholars of Saveetha Dental College and Hospitals, Saveetha Institute of Medical and Technical Sciences, Chennai for their cooperation throughout the work.

**ACSIA REGI J**

## TABLE OF CONTENTS

S.NO.	TITLE	PAGE NUMBER
1.	ABSTRACT	1
2.	INTRODUCTION	3
3.	SCOPE OF THE WORK	13
4.	MATERIALS AND METHODS	15
5.	ELECTRODE FABRICATION	18
6.	RESULTS AND DISCUSSIONS	21
7.	CONCLUSION	28
8.	REFERENCE	30

## LIST OF FIGURES

- Figure 1:** Schematic structure of a chemical sensor.
- Figure 2:** Classification of chemical sensors based on sensing objects.
- Figure 3:** Schematic illustration of the basic components of an electrochemical sensor.
- Figure 4:** Nitrofurantoin.
- Figure 5:** Crystallographic unit cell arrangement in  $\text{MnO}_2$ .
- Figure 6:** Structures of (a)  $\alpha$ - $\text{MnO}_2$ , (b)  $\beta$ - $\text{MnO}_2$ , (c)  $\gamma$ - $\text{MnO}_2$ , (d)  $\delta$ - $\text{MnO}_2$ , (e)  $\lambda$ - $\text{MnO}_2$ .  
Pink and Red spheres represent Mn and O atoms respectively.
- Figure 7:** Illustration of edge shape and nomenclature for armchair and zigzag GNRs.
- Figure 8:** Images of (a) UV-Visible spectrophotometer (UV), (b) X-ray diffraction spectrometer (XRD), (c) HI-Resolution scanning electron microscope, (d) HI-Resolution transmission electron microscope, (e) Electrochemical workstation-CH instrument.
- Figure 9:** UV-visible absorption (UV-vis) spectrum of GNR,  $\text{MnO}_2$ , GNR/ $\text{MnO}_2$ .
- Figure 10:** The XRD for the analysis of (a) GNR, (b)  $\alpha$ - $\text{MnO}_2$ , and (c) GNR/ $\text{MnO}_2$  composite.
- Figure 11:** HR-SEM and HR-TEM images of (a) agglomerated pristine MWCNT, (b) HR-TEM images of unzipped MWCNT, (c) morphology of  $\text{MnO}_2$  nanoplates.
- Figure 12:** (a) Comparison CVs of bare and upon the addition of 200 nm of NFT, (b)  $\text{MnO}_2$  modified GCE for the analysis of NFT (c) GNR/ $\text{MnO}_2$ /GCE modified GCE for the analysis of NFT in 0.1 M phosphate buffer solution at the scan rate of 50 mV/s.
- Figure 13:** a) CVs for the concentration analysis of NFT in 0.1 phosphate buffer solution from 1-900 nM, at the scan rate of 50 mV/s, and (b) The relationship between the

concentration of NFT vs the reduction current ( $I_{pc}$ ).

**Figure 14:** The interference analysis was done with the NFT using the GNR/MnO<sub>2</sub>/GCE.

## LIST OF ABBREVIATIONS

<b>NFT</b>	Nitrofurantoin
<b>GNR</b>	Graphene Nanoribbon
<b>MWCNT</b>	Multi-Walled Carbon Nanotubes
<b>LOD</b>	Limit of Detection
<b>NPs</b>	Nanoparticles



## ABSTRACT

The discovery of antibiotics is the greatest revolution for the worldwide modern research society and the healthcare system. Especially, nitrofurantoin (NFT) belongs to the class of the nitrofuran derivative and owns a broad spectrum of activity as an antibacterial agent of the food additive in livestock and aquatic product. NFT is the most frequently used drug for pregnant women for the treatment of urinary tract infections but with the side effect of direct affection on the child's red blood cells. Therefore, it is most important to monitor the level of NFT in humans. Herein, a nanocomposite of 1D Graphene nanoribbon/Manganese dioxide nanoplates (GNR/MnO<sub>2</sub>) was prepared using the top-down method and then used to fabricate an electrochemical NFT sensor. The manganese dioxide (MnO<sub>2</sub>) was synthesized by the hydrothermal method. The GNR was synthesized by oxidative unzipping of multi-walled carbon nanotubes (MWCNTs). The nanocomposite was characterized by UV-Visible (UV-Vis), XRD, HR-SEM and HR-TEM images. The obtained product of GNR/MnO<sub>2</sub> was studied using cyclic voltammetry (CV) showed a redox peak around 0.9 and 0.6 V in phosphate buffer solution. The NFT electrochemical reduction was performed with GNR/MnO<sub>2</sub> modified electrode. The electrochemical studies revealed that the NFT reduction occurs at a potential of -0.38 V. Also, the concentration study from the CV measurement for NFT reduction and the linear range obtained was from 1 - 900 nM and the limit of detection (LOD) was calculated to be 0.3 nM. The selectivity was also studied for NFT reduction with other interferents. We conclude that the proposed GNR/MnO<sub>2</sub> modified electrode demonstrated excellent stability and selectivity for NFT detection.

**Keywords:** Graphene nanoribbon, MnO<sub>2</sub>, Nitrofurantoin, Electrochemical sensors.

# **CHAPTER 1**

# 1. INTRODUCTION

## 1.1. SENSORS

A sensor is often defined as a device that receives and responds to a signal or stimulus. The stimulus is the quantity, property, or condition that is sensed, and converted into an electrical signal. We may say that a sensor is a translator of a generally non-electrical value into an electrical value. When we say “electrical”, we mean a signal which can be channeled, electrified, and amplified by electronic devices. The sensor’s output signal may be in the form of voltage, current, or charge [1]. Chemical sensors are devices that transform chemical information, ranging from the concentration of a specific sample component to overall composition analysis, into an analytically useful signal [2]. The chemical sensors are typically made of two main components: the sensing material and the transducer. The sensing material is in charge to interact with the target analyte, and the consequence of this binding interaction is the change of material property, such as mass and electrical conductivity. The transducer then translates this change into a readable signal, usually an electronic signal (**Fig. 1**) [3].

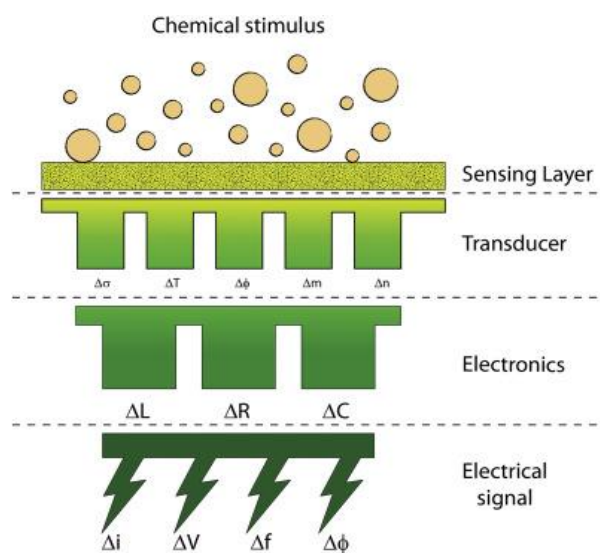


**Fig. 1.** Schematic structure of a chemical sensor.

According to the working principle, the chemical sensor can be classified into many types such as optical, electrochemical, mass, magnetic, and thermal. Another way to categorize the chemical sensors is based on the object to be detected, that is, the chemical sensors can be classified as gas sensors for trace gas analysis and monitoring, various ion sensors represented by the pH sensor, humidity sensor, and biosensors made by biological characteristics (**Fig. 2**).

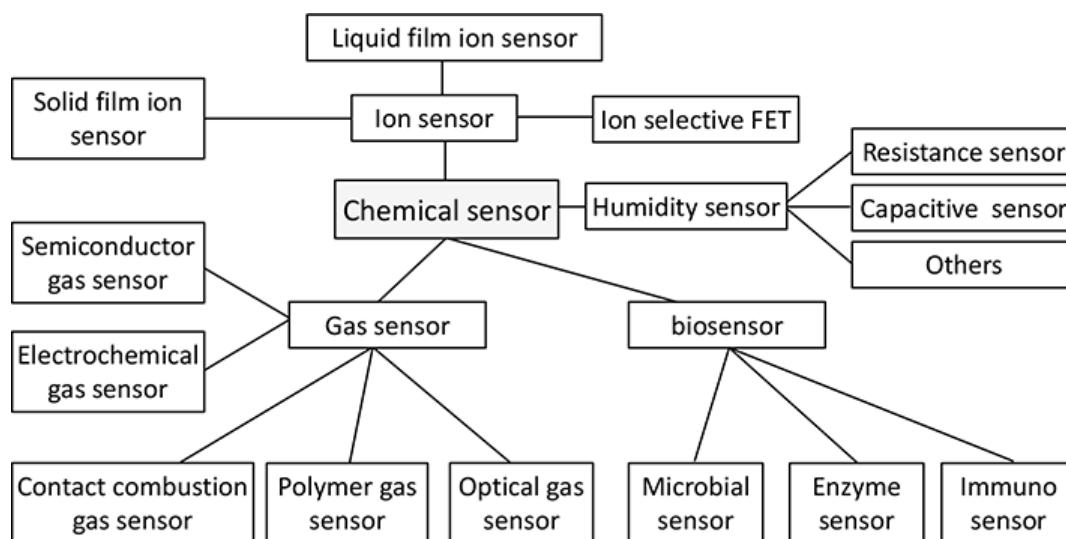


**Fig. 2.** Classification of chemical sensors based on sensing objects.

In the electrochemical sensor, the measured output signal should be in the form of current, voltage, resistance, or capacitance. The electrochemical sensors are broadly classified into two categories namely chemical sensors and biosensors. If the active element of the sensor is a biomolecule, converting or catalyzing the (bio) chemical reaction into a measurable signal is known as an electrochemical biosensor. Although the history of chemical sensors dates back not long ago, it has gained increasing attraction for applications in environmental monitoring, industrial process monitoring, gas composition analysis, medicine, and on-site emergency disposal owing to its many excellent properties such as small size, satisfactory sensitivity, larger dynamic range, low cost, and easy to realize automatic measurement [4].

## 1.2. ELECTROCHEMICAL SENSORS

Electrochemical sensors are the quickest growing field of chemical sensors [5]. They are made up of three essential components: a **receptor** that binds the sample, the **sample, or the analyte**, and a **transducer** to convert the reaction into a measurable electrical signal. In the case of electrochemical sensors, the modified electrode acts as the transducer (**Fig. 3**) [6].

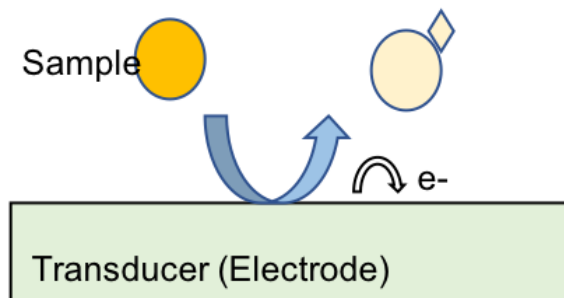


**Fig. 3.** Schematic illustration of the basic components of an electrochemical sensor.

The current-type electrochemical sensor is based on the detection system that consists of the counter electrode, reference electrode, and working electrode. The redox reaction between the tested substance and the sensitive material takes place on the surface of the working electrode, which results in the variation of current [7]. In most electrochemical sensors, an electrode surface is used as the site of the reaction. The electrode will either oxidize or reduce the analyte of interest. The current that is produced from the reaction is monitored and used to calculate important data such as concentrations from the sample[6].

These sensors are notable because of several factors: the use of the electron for signal acquisition, which is considered a clean model for analytical applications, with no generation of waste; miniaturization in portable devices (analyses with microvolumes of samples); fast analysis; and low production cost, allowing the popularization of these methods (e.g., as commercial glucose sensors)[8]. Additionally, the preparation of electrochemical sensors is simple, easy to handle, and catalyst material can be reused multiple times [9].

### 1.3. NITROFURANTOIN

Nitrofurantoin [(NFT)-*N*-(5-nitro-2-furfurylidene)-1-aminohydantoin], with the molecular formula:  $C_8H_6N_4O_5$  [10], is described as lemon-yellow crystals or powder with a bitter taste [11] and is a well-known antimicrobial drug that has been shown to actively inhibit several gram-positive as well as gram-negative microbes[12]. Nitrofurantoin (NFT) (**Fig. 4**) is a member of the nitrofurans family. The defining structural component is a furan ring [five-membered aromatic ring with four carbon (C) atoms and one oxygen (O)] directly connected to a nitro group ( $-NO_2$ ) [13].

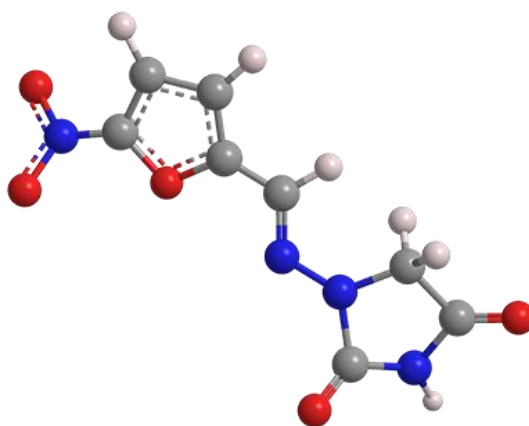


**Fig. 4.** Nitrofurantoin

The nitrofurans derivative nitrofurantoin has been used for more than 60 years for the antibacterial therapy of uncomplicated urinary tract infections (UTI) [14]. It has also been associated with patients with neuropathy, hepatitis, pulmonary fibrosis, and hemolytic anemia suffering from the deficiency of glucose-6-phosphate [12]. The nitrofurans furazolidone, furaltadone, nitrofurantoin, and nitrofurazone (which contain a characteristic 5-nitrofurans ring) were commonly employed as feed additives for growth promotion and, to prevent bacterial and protozoan infections to livestock, aquaculture, and bee colonies[15]. The broad application of NTF demands the researchers to develop a fast and sensitive analytical technique for detection of the trace substance [16]. Despite having such excellent antimicrobial activity, NFT showed some amount of metabolic toxicity. NFT also has the versatile ability in generating reactive species of oxygen and NO through its nitro group reduction. Where, by all these factors NFT is vividly released into environmental habitats making the contamination in the

ecosystem, even at a quite low amount of level it is harmful and dangerous. So, to overcome the exposure monitoring of NFT in the environment, food and pharmaceutical levels are necessary for avoiding the risk which is associated. It is a necessity to develop a highly sensitive, accurate, and rapid real-time analytical tool to detect the presence of NFT. In pursuit of this goal, several methods have already been reported for the determination of NFT such as colorimetry, spectrophotometry, polarography, high-performance liquid chromatography (HPLC), and reductive flow-injection amperometry. However, these methods did not provide a satisfactory quantification limit for detection[12].

#### 1.4. MnO<sub>2</sub>

MnO<sub>2</sub> is an inexpensive and environmentally friendly multi-functional material, which has been used in numerous applications[17]. Crystallographically, MnO<sub>2</sub> can have many polymorphic forms, such as  $\alpha$ -,  $\beta$ -,  $\gamma$ -,  $\delta$ -, and  $\lambda$ - MnO<sub>2</sub> [18], which are made of the basic structure unit [MnO<sub>6</sub>] octahedron with different connectivity. According to different [MnO<sub>6</sub>] octahedron links, the MnO<sub>2</sub> structures can be divided into chain-like tunnel structures and sheet or layered structures [19]. The polymorphs have distinctive atomic arrangements that result in various types of pores or tunnels within the crystal structure. Due to the distinctive crystal structure, the selectivity toward different ions or electron transfer kinetics is immense[20].

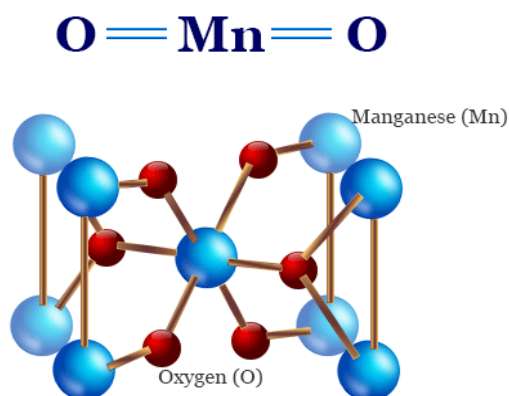


**Fig. 5.** Crystallographic unit cell arrangement in MnO<sub>2</sub>

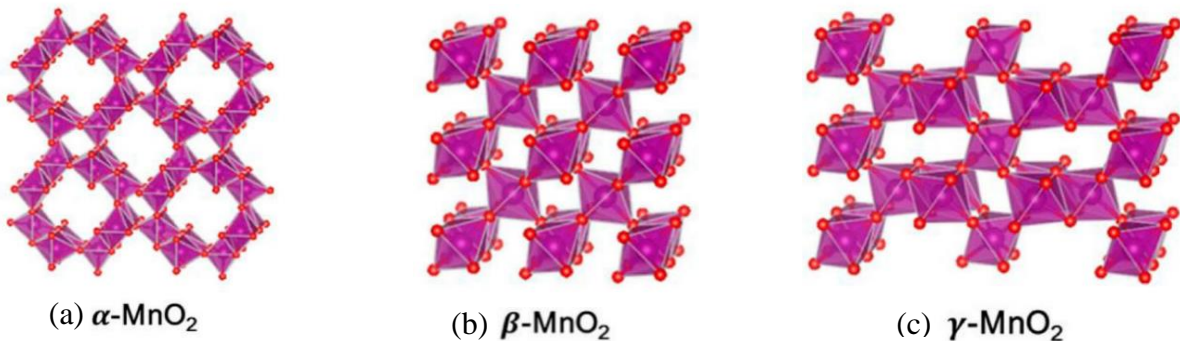
**$\alpha$ -MnO<sub>2</sub>:** The **Fig. 6(a)**  $\alpha$ -MnO<sub>2</sub> consists of interlinking double chains of MnO<sub>6</sub> octahedra and an interstitial space composed of 1D tunnels with relative dimensions 2 2 and 1 1 that extend along the c-axis of the tetragonal unit cell. The continuous extension of MnO<sub>6</sub> octahedra along the c-axis direction can lead to the preferred growth of MnO<sub>2</sub> along with the [001] direction. 1D MnO<sub>2</sub> includes nanorods, nanofibers, nanoneedles, nanotubes, and nanowires. The attractive properties of 1D MnO<sub>2</sub> are efficient electron transportation and excitation along the longitudinal pathway with outstanding mechanical strength. Hence, 1D nanostructure has been widely used in the field of electrical, optical, sensor, and photocatalysis

**$\beta$ - MnO<sub>2</sub>:** It is composed of a single strand of edge-sharing MnO<sub>6</sub> octahedral to form a 1D (1×1) tunnel **Fig. 6(b)**. And it is found that  $\beta$ -MnO<sub>2</sub> is one of the metal oxides which are easier to be present as nanowires.

**$\gamma$ - MnO<sub>2</sub>:** It is a random intergrowth of ramsdellite an orthorhombic manganese dioxide mineral, usually found in deposits containing other manganese oxide crystals (1×2) and pyrolusite a common manganese mineral that constitutes an important ore, it is black amorphous and often granular, fibrous, found as reniform crusts or in columnar structure, (1×1) domains **Fig. 6(c)**.

**$\delta$ -MnO<sub>2</sub>:** This has a layer structure, with sheets made from manganese-oxygen octahedra, separated by alkali or other ions, and water. It has a  $\sim 7$  Å interlayer separation and it is a 2D compound **Fig. 6(d)** [20].

**$\lambda$ -MnO<sub>2</sub>:** It is a 3D spinel structure **Fig. 6(e)**. A metastable form of manganese dioxide [21].





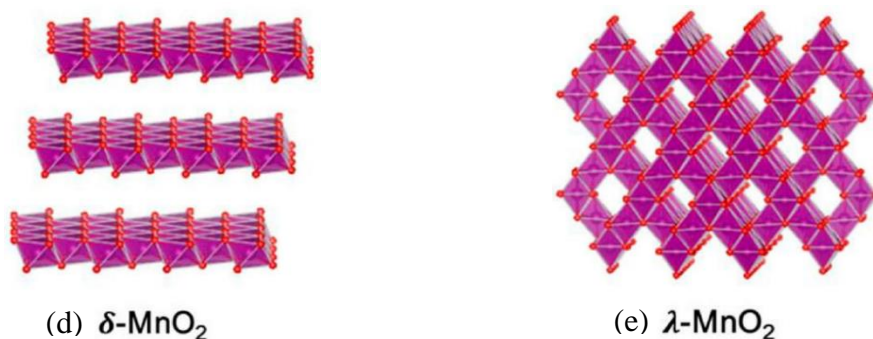


**Fig. 6:** Structures of (a)  $\alpha\text{-MnO}_2$ , (b)  $\beta\text{-MnO}_2$ , (c)  $\gamma\text{-MnO}_2$ , (d)  $\delta\text{-MnO}_2$ , (e)  $\lambda\text{-MnO}_2$ . Pink and red spheres represent Mn, and O atoms, respectively[22].

In the comparative study of oxidation over  $\alpha$ -,  $\beta$ -,  $\gamma$ -,  $\delta$ -, and  $\lambda$ -  $\text{MnO}_2$ , it was found that the oxidation activity of catalysts decreased in the order of  $\alpha\text{-MnO}_2 > \delta\text{-MnO}_2 > \gamma\text{-MnO}_2 > \beta\text{-MnO}_2$  [23]. Among all the transition metal oxides,  $\text{MnO}_2$  has a relatively high catalytic activity in the catalytic decomposition of organic compounds by oxidation [23].  $\text{MnO}_2$  has many uses, including the manufacture of batteries, beverage cans, agricultural pesticides and fungicides, and electronic circuitry[24].

## 1.5. GRAPHENE NANORIBBON

Graphene nanoribbons (GNRs) are a family of one-dimensional (1D) materials with a graphitic lattice structure[25]. Graphene nanoribbons are a highly developed form of graphene with wide importance due to their distinctive properties such as large surface area, enhanced mechanical strength, and improved electro-conductivity[26]. They are generally categorized by the structure of their long edges, which can have an armchair, a zigzag, or an intermediate character.

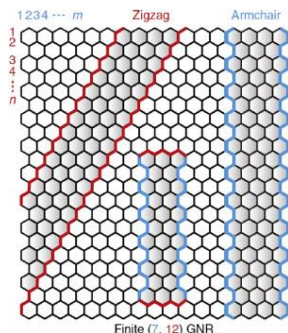


**Fig.7.** Illustration of edge shape and nomenclature for armchair and zigzag GNRs.

The edge structure has profound implications for the electronic properties of the GNRs [27]. Graphene nanoribbons have been largely studied theoretically, experimentally, and with the perspective of electronic applications [28]. Graphene nanoribbons in comparison with carbon nanotubes, have reactive edges which can increase the adsorption and electrocatalysis of certain molecules which are used as a promising electrode material[29].

It is well known that the activity and durability of a catalyst are highly dependent on the structure and composition of the support in addition to those of metallic nanoparticles. Supported catalysts decrease the usage of noble metals and expose more surface-active sites due to their higher dispersion state, moreover, a synergistic effect between the metals and the supports may be enabled owing to their electronic interaction. So far, materials including carbon black, carbon microspheres, carbon nanotubes, and graphene, have widely been employed as supporting materials. Specifically, multi-walled carbon nanotubes (MWCNTs) have drawn significant attention in electrocatalysis since they possess a larger surface area and a higher electrical conductivity. Compared to MWCNTs, GNRs can provide oxy-groups to facilitate uniform deposition of metallic nanoparticles (NPs) and facile dispersion of the GNRs-supported catalysts in aqueous solvents, and thus are a new type of supporting carbon materials for novel electrocatalysts[30].

## LITERATURE REVIEW

**B. He, J. Li.** reported a sensitive electrochemical sensor based on reduced graphene oxide/Fe<sub>3</sub>O<sub>4</sub> nanorods composites for detection of nitrofurantoin and its metabolite[31].

In 2019 **S.V. Selvi *et al.*** had reported detection of nitrofurantoin in biological samples using graphene/tungsten trioxide (Gr/WO<sub>3</sub>) composite modified screen-printed carbon electrode[32].

**K.-Y. Hwa *et al.*** prepared a nano-assembly of NiFe spheres anchored on f-MWCNT for electrocatalytic reduction and sensing of nitrofurantoin in biological samples[12].

**Zhi-Liang Wu *et al.*** reported the facile hydrothermal preparation of MnO<sub>2</sub>/reduced graphene oxide nanoribbons and application of in amperometric detection of hydrogen peroxide[33].

**Q. Liu *et al.*** reported the synthesis of manganese dioxide coated graphene nanoribbons supported palladium nanoparticles as an efficient catalyst for ethanol electrooxidation in alkaline media[30].

# **CHAPTER 2**

## 2. SCOPE OF THE WORK

From the literature survey, it was identified that there are different methods for the synthesis of nanoparticles: such as coprecipitation, solid-phase synthesis, inert gas condensation, ion sputtering, scattering, microemulsion, microwave, pulse laser ablation, sol-gel, sonochemical, spark discharge, template synthesis, and biological synthesis[34]. The above-mentioned methodologies had some limitations in the product conversion, yield, impurities of the foreign molecule, and unreacted molecule[35].

In hydrothermal synthesis, the chemical purity of the powder materials is higher due to starting with high purity precursors. During crystallization processes, growing crystals/crystallites tend to reject impurities present in the growth environment. Therefore, it is expected that impurities such as ions that come from metal salts or pH adjusting agents are removed from the system together with the crystallization solution [36]. And the reaction parameters, such as the type and concentration of the precursors, the solvent, the stabilizing agents, and the reaction temperature and time, present important effects on the products[37]. The novel synthesis of  $\text{MnO}_2$  is based on the methodology.

From the ideas and observation, the synthesis of  $\text{MnO}_2$  by the hydrothermal methodology. The method of synthesis avoids the traditional methodology of solvent usage and the duration of the reaction. The material was confirmed using UV-Visible spectroscopy (UV). The crystal structure and phase of the as-prepared materials were characterized by X-ray diffraction (XRD). A scanning electron microscopy (SEM) was used to study the morphologies and microstructures of the samples. A schematic representation of the structural evolution of nanoribbons, as well as the corresponding transmission electron microscopy (TEM).

.

# **CHAPTER 3**

### 3. MATERIALS AND METHODS

#### 3.1. THE HYDROTHERMAL SYNTHESIS OF MnO<sub>2</sub>

MnO<sub>2</sub>, MWCNTs, hydrogen peroxide (H<sub>2</sub>O<sub>2</sub>) and potassium permanganate (KMnO<sub>4</sub>) purchased from sigma-Aldrich. The monosodium hydrogen phosphate (NaH<sub>2</sub>PO<sub>4</sub>) and disodium hydrogen phosphate (Na<sub>2</sub>HPO<sub>4</sub>) obtained from SRL India. The phosphate buffer electrolyte solution prepared using NaH<sub>2</sub>PO<sub>4</sub> and Na<sub>2</sub>HPO<sub>4</sub> (pH=7) for the sensing of nitrofurantoin. All the experiments done with the milli-Q-water (18.2 MΩ.cm @ 25±2°C).

The electrochemical studies are carried out with the three-electrode system – Electrochemical workstation - CH Instruments, USA (Model: CHI-760E). Cyclic voltammetry is an electrochemical potentiodynamic measurement that allows studying the redox property of compounds for obtaining the stability of reaction and interfacial structure. CV is performed by cycling the potential of a working electrode and measuring the resulting current that is developed in the electrochemical cell. The current due to the reduction process is observed during the forward scan and those due to oxidation on the reverse scan.

The material was confirmed using UV-Visible spectroscopy (UV). The phase purity of synthesized materials was studied using X-ray diffraction (XRD). The particle morphology and structural properties of the prepared MnO<sub>2</sub> were further elucidated by scanning electron microscopy (SEM). A schematic representation of the structural evolution of nanoribbons was studied using the transmission electron microscopy (TEM) images. All the experiments were done at room temperature (25±0.2°C).

### 3.2. INSTRUMENTS



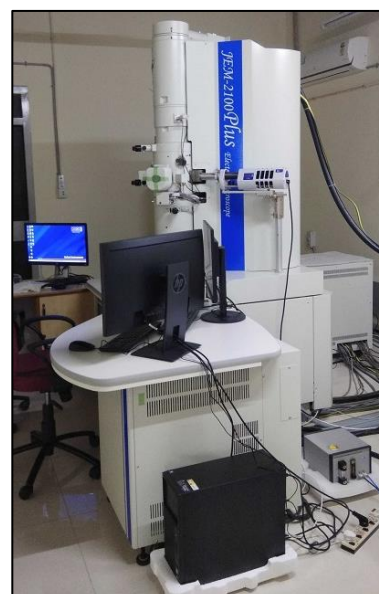
**(a) UV-VIS SPECTROPHOTOMETER**



**(b) X-RAY DIFFRACTION SPECTROMETER**



**(c) HI-RESOLUTION SCANNING ELECTRON MICROSCOPE**



**(d) HI-RESOLUTION TRANSMISSION ELECTRON MICROSCOPE**



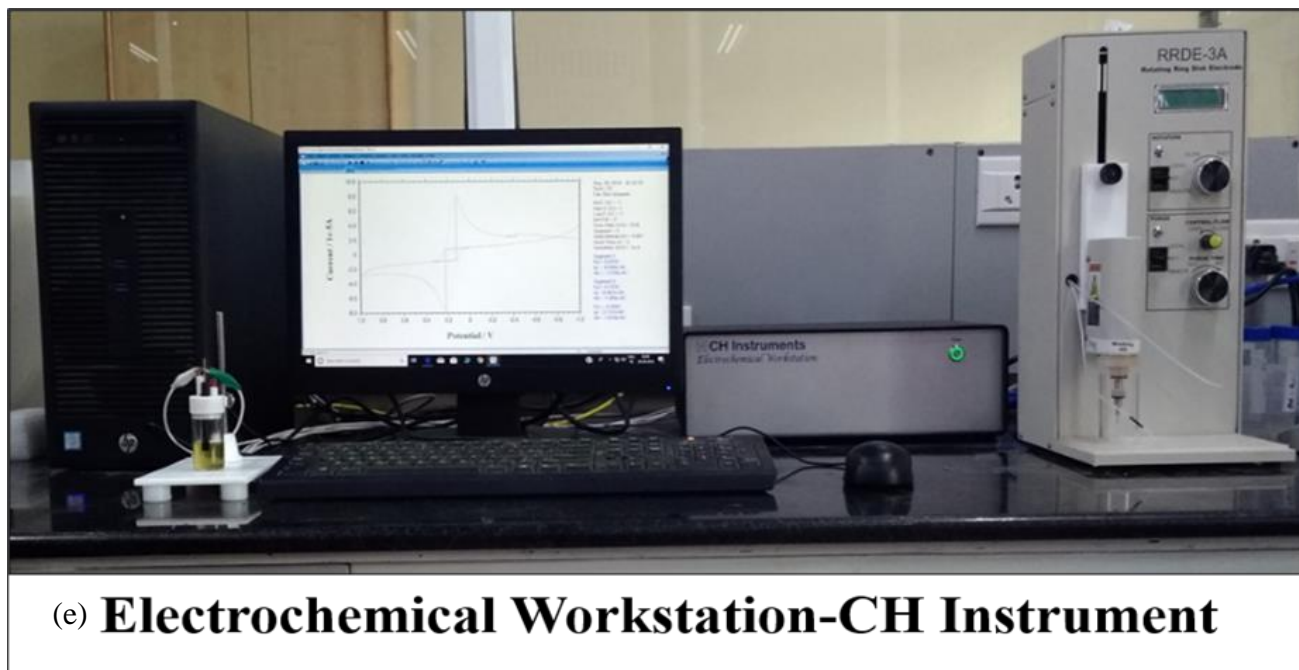


**Fig.8.** Images of (a) UV-Visible spectrophotometer (UV), (b) X-ray diffraction spectrometer (XRD), (c) HI-Resolution scanning electron microscope, (d) HI-Resolution transmission electron microscope, (e) Electrochemical workstation-CH instrument.

### 3.3. UNZIPPING OF MWCNTs

Multi-Walled Carbon Nanotubes (MWCNTs) are hollow, cylindrically shaped allotropes of carbon that have a high aspect ratio (length to diameter ratio). Their name is derived from their structure and the walls are formed by multiple one-atom-thick sheets of carbon and graphene nanoribbons (GNRs) are narrow strips of graphene with a very high length-to-width ratio. GNRs were prepared by longitudinal unzipping of the pristine MWCNTs.

0.025 mg of MWCNTs was taken, 7.5 ml of sulfuric acid was added to it and then the mixture was placed and kept for magnetic stirring at room temperature for 3 hours. After adding potassium permanganate ( $\text{KMnO}_4$ ) to the solution its temperature was maintained below  $10^\circ\text{C}$  for 2 hours. There is a rise in temperature up to  $35^\circ\text{C}$  for 30 mins and further increased up to  $75^\circ$  for the next 30 minutes. The solution is then added to 300 ml of ice water containing 10 ml of  $\text{H}_2\text{O}_2$ . Then it is filtered and washed until it reaches neutral pH. The product obtained is kept in the vacuum oven at  $60^\circ\text{C}$  for 10 hours

### 3.4. Synthesis of MnO<sub>2</sub> nanoplates

Synthesis of MnO<sub>2</sub> nanoplate was carried out hydrothermally starting with MnCl<sub>2</sub> (4 mM) dissolved in 40 mL ethanol, 3 mL H<sub>2</sub>O under constant stirring at 1100 rpm for 30 minutes. Then sodium acetate the reducing agent was added to the above solution. The mixture was kept in constant stirring and then transferred to a steel line autoclave. The reaction was kept at 180°C for 12 h. The pressure vessel was allowed to cool to room temperature naturally. The precipitate formed was filtered and washed copiously with ethanol and distilled water until all the unreacted materials were removed. After that, the resultant product was kept calcination for 2 h at 150°C, and the dark brown MnO<sub>2</sub> was obtained.

### 3.5. Synthesis of GNR/MnO<sub>2</sub> nanoplates nanocomposite

Synthesis of GNR/MnO<sub>2</sub> nanoplate was carried out hydrothermally starting with MnCl<sub>2</sub> (4 mM) dissolved in 40 mL ethanol, GNR and water (3 mL). Then sodium acetate the reducing agent was added to the above solution. The mixture was stirred for 20 min at room temperature and then transferred into a 100 mL Teflon-lined stainless-steel autoclave and loaded into an oven. It was then heated at 180° C for 12hrs. The pressure vessel was allowed to cool to room temperature naturally. The precipitate formed was filtered and washed copiously with ethanol and distilled water until all the unreacted materials were removed. After that, the prepared nanocomposite was calcinated for 2 hr. at 150° C the GNR / MnO<sub>2</sub> nanocomposite was obtained.

### 3.6. ELECTRODE FABRICATION PROCESS

To conduct electrochemical studies, three-electrode setup with unmodified and GNR/MnO<sub>2</sub> nanocomposite modified electrode was used as a working electrode; Ag/AgCl as a reference electrode and platinum wire as the auxiliary electrode. The working electrode was polished with an electrode polishing pad with the sequence of alumina powder (Al<sub>2</sub>O<sub>3</sub>, sizes with ~1 μm, ~0.3 μm, and ~0.05 μm). Next, the GCE was washed in ultrapure Milli-Q water and left to air dry at room temperature. After that, 10 μL of homogeneous GNR/MnO<sub>2</sub> nanocomposite dispersion was drop casted on the electrode surface and left to dry. To remove the unbounded particles, the GNR/MnO<sub>2</sub>/GCE was rinsed with distilled water. Also, GNR/GCE and MnO<sub>2</sub>/GCE were prepared in the same way for the experiments.

For the working electrode modification, the procedure to be followed: The obtained material  $\text{MnO}_2$  (1 mg) catalyst was dispersed in distilled water using sonication. The product was not dispersed well. After sonication, the supernatant solution was used for all sensing applications. Before each experiment, the solution was sonicated for 30 minutes. Then, 3  $\mu\text{L}$  of redispersed material was coated on the GCE and dried at  $50^\circ\text{C}$  for 5 minutes. For checking electrochemical activity, each experiment before the electrolyte- 0.1 M phosphate buffer solution was purged with nitrogen to remove the dissolved oxygen. The  $\text{MnO}_2$  modified electrode was cycled in the reduction potential window from 1.2 to -0.8 V at the scan rate of 50 mV/s. The comparative material studies also followed the same procedure as the CV studies. For analyzing nitrofurantoin, the effect of scan rate for material, concentration studies for nitrofurantoin, and interference analysis with nitrofurantoin were studied in the same potential range of 1.2 to -0.8 V.

# **CHAPTER 4**

## 4. RESULTS AND DISCUSSION

### 4.1. CHARACTERISATION

#### 4.1.1. UV-Vis spectrum

The **Fig. 9**. black curve UV–Vis spectra of GNR dispersion showed a strong absorbance band at 250 nm, which denotes the  $\pi$ – $\pi^*$  transition of aromatic C–C bonds can be assigned to the partially oxidized graphene nanoribbons. The red curve denoted  $\text{MnO}_2$  two absorption peaks at 284 and 389 nm each of which is related to the bandgap absorption of the  $\text{MnO}_2$  nanoplates (NPs). The absorption peak at 380 nm is attributed to the d–d transitions of Mn ions in  $\text{MnO}_2$  NPs. The blue curve denotes GNR/ $\text{MnO}_2$  nanocomposite the absorbance peak is shifted from 284 to 290 nm and 389 to 400 nm. Such a shifting of absorbance toward higher wavelength indicates that there could be a strong interaction between  $\text{MnO}_2$  NPs and GNR, resulting in the formation of GNR/ $\text{MnO}_2$  nanocomposite.

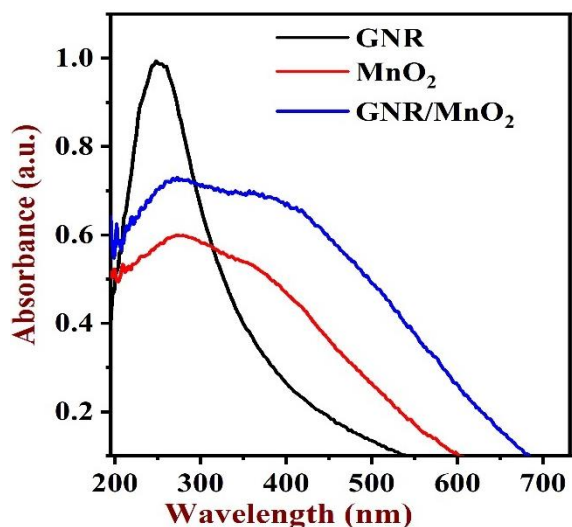


**Fig. 9.** UV–visible absorption (UV–vis) spectra of GNR,  $\text{MnO}_2$ , GNR/ $\text{MnO}_2$ .

#### 4.1.2. XRD

The crystal phase and structure of the products were obtained by XRD. This product is monitored by XRD (see **Fig.10(a)**), the pattern shows two diffraction peaks, one at  $2\theta=25.4^\circ$  (corresponding to (002) crystal plane), and another at  $42.8^\circ$  (corresponding to (100) crystal plane). The broad sawtooth-shaped reflection at  $42.8^\circ$  indicates that GNRs exhibit turbostratic disorder. In **Fig. 10(b)**

the typical reflection peaks of  $\alpha$ -MnO<sub>2</sub> are observed at  $2\theta$  values of 18.0°, 28.6°, 36.7°, 38.6°, 41.9°, 49.7°, 56.4°, 60.2°, 65.4°, 69.6°, and 72.9° corresponding to (200), (310), (400), (211), (420), (301), (600), (521), (002), (541), and (312) planes of  $\alpha$ -MnO<sub>2</sub> crystals. In **Fig.10(c)** the major peak of GNR and MnO<sub>2</sub> were found where positive shift is observed. This denoted that the formation of GNR/MnO<sub>2</sub> composite have been successfully formed with increased catalytic effect. This can be due the electrostatic charge attraction between the GNR and MnO<sub>2</sub> dispersion.

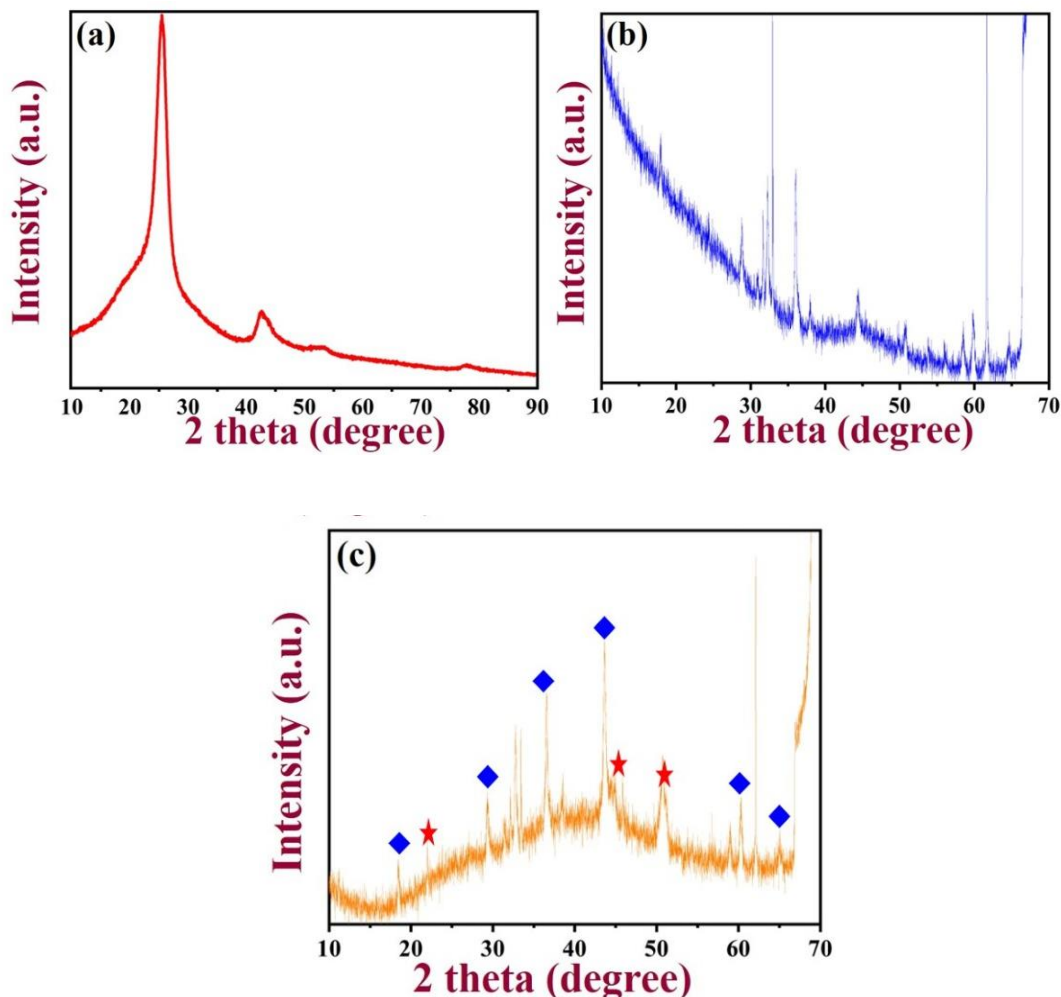


**Fig. 10.** The XRD for the analysis of (a) GNR, (b)  $\alpha$ -MnO<sub>2</sub> and (c) GNR/MnO<sub>2</sub> composite.

#### 4.1.3. HR-SEM and HR-TEM

The morphology of GNR and MnO<sub>2</sub> were studied using HR-SEM and HR-TEM as shown in **Fig. 11**. **Fig.11(a)** shows the agglomerated pristine MWCNT, which was taken by dispersing the MWCNT in aqueous medium. The diameter of the tubes was found to be in 20-30 nm in range.

Then **Fig.11(b)** shows the HR-TEM images of unzipped MWCNT whose diameter was found to be increased showing the unzipping of MWCNT was taken place successfully. The **Fig.11(c)** shows the morphology of MnO<sub>2</sub> nanoplates.

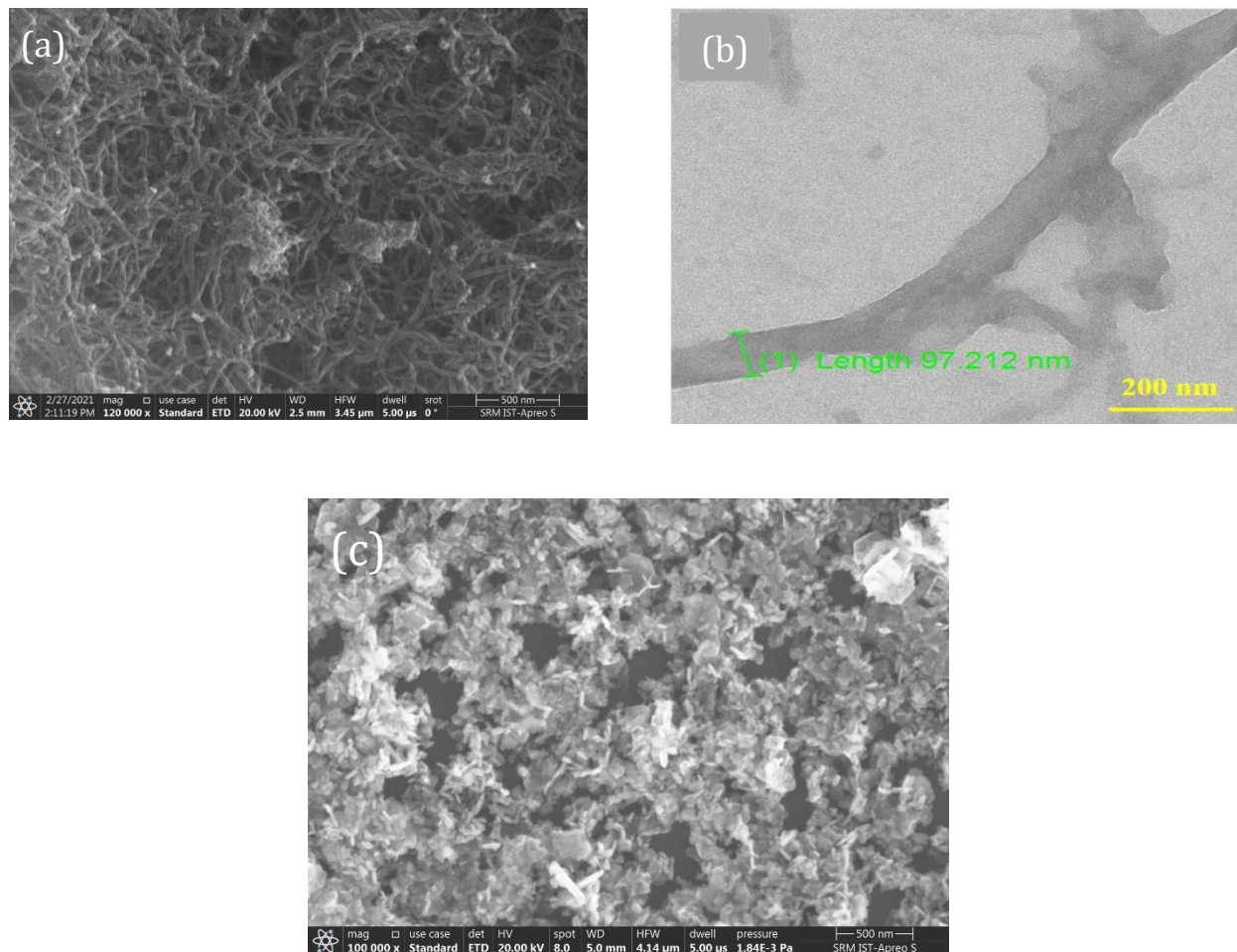


**Fig.11.** HR-SEM and HR-TEM images of (a) agglomerated pristine MWCNT, (b) HR-TEM images of GNR, and (c) morphology of MnO<sub>2</sub> nanoplates.

## 4.2. Electrochemical studies

The catalytic activity of GNR/MnO<sub>2</sub> modified GCE was studied using CV. The **Fig.12(a)** shows the CV's of bare GCE in 0.1M PBS at a scan of 50 mV/s (black Curve). Upon the addition of 200 nm of NFT shows an increase in the cathodic current (1.7  $\mu$ A) at -0.42 V. This experiment was maintained in the nitrogen saturated solution (red curve). Then the modified GNR/GCE was studies with the presence 200 nm of NF 0.1M PBS at a scan of 50 mV/s, which should the catalytic

current response of  $2.1 \mu\text{A}$  at  $-0.32 \text{ V}$ . When compared with the bare GCE the over potential of GNR/GCE has been reduced up to  $10 \text{ mV}$  during the reaction. Later the  $\text{MnO}_2$  modified GCE was studied using CV technique in the nitrogen atmosphere whose CV's were recorded in  $0.1 \text{ M}$  PBS at a scan of  $50 \text{ mV/s}$ . The  $\text{MnO}_2$  modified GCE showed the redox peak at  $0.9$  and  $0.6 \text{ V}$  in  $0.1 \text{ M}$  PBS and the formal potential to be  $0.75 \text{ V}$  (**Fig.12(b)**). Finally, the GNR/ $\text{MnO}_2$ /GCE was tested with the presence of  $200 \text{ nm}$  of NFT in the nitrogen atmosphere in  $0.1 \text{ M}$  PBS at a scan rate of  $50 \text{ mV/s}$  **Fig.12(c)**. The overall modified GCE's onset potential and the cathodic currents are mentioned in the table.

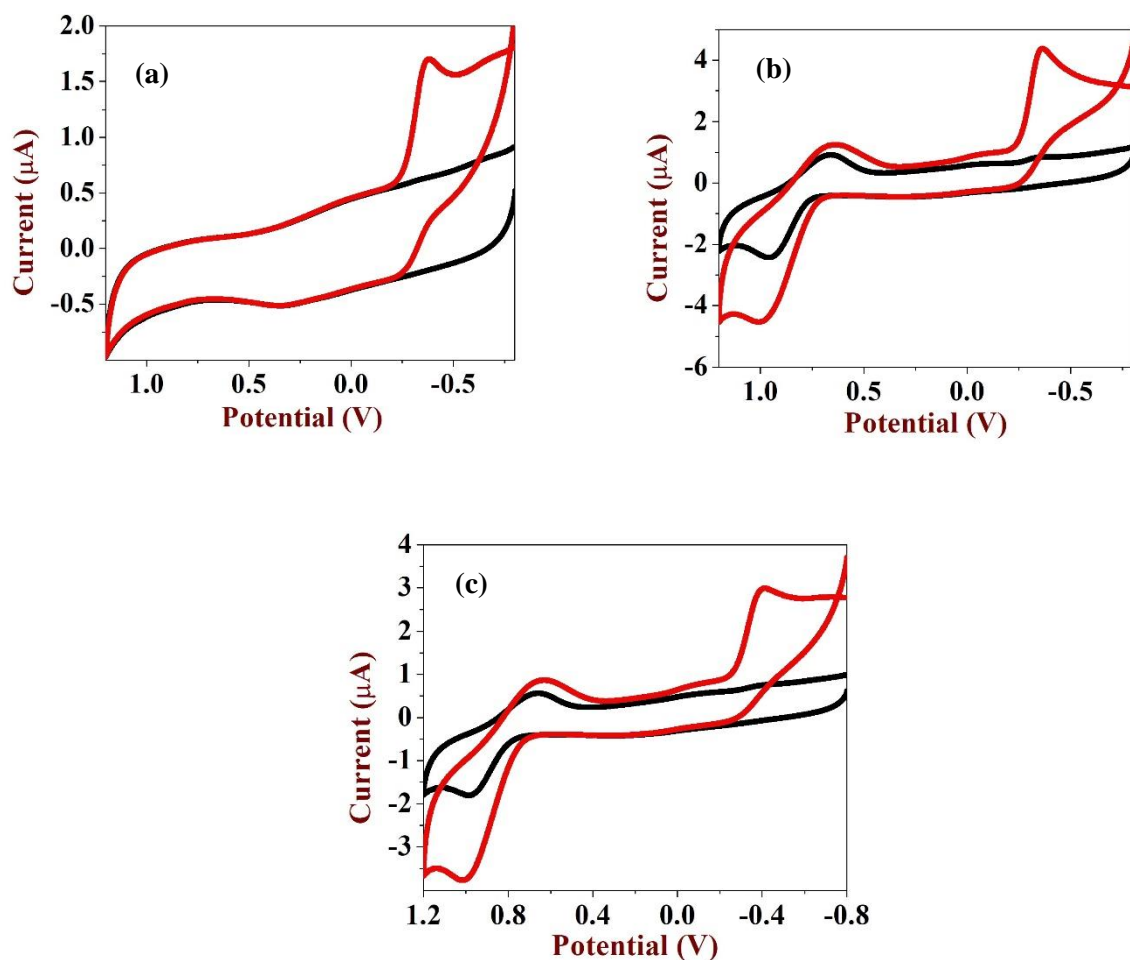


**Fig.12.** (a) Comparison CVs of bare and upon the addition of  $200 \text{ nm}$  of NFT, (b)  $\text{MnO}_2$  modified GCE for the analysis NFT, (c) GNR/ $\text{MnO}_2$ /GCE modified GCE for the analysis NFT in  $0.1 \text{ M}$  phosphate buffer solution at the scan rate of  $50 \text{ mV/s}$ .



**Table.1.** The different modified electrodes onset potential and cathodic current measured in 0.1 M PBS at a scan rate of 50 mV/s.

S.No.	Electrodes	Onset potential	Cathodic current ( $\mu\text{A}$ )
1	Bare electrode	-0.42	1.70
2	$\text{MnO}_2/\text{GCE}$	-0.41	2.4
3	$\text{GNR}/\text{GCE}$	-0.32	2.1
4	$\text{MnO}_2/\text{GNR}/\text{GCE}$	-0.38	3.2

#### 4.3. Concentration studies

The analysis of NFT on the modified  $\text{GNR}/\text{MnO}_2/\text{GCE}$  in 0.1 M phosphate buffer solution was carried out, the reduction process takes place and the corresponding current increases at the oxidation potential of Mn (0.925 V) was observed after the addition of 100 nM concentrations of NFT. In **(Fig. 13(a))**, the concentration was increased linearly from 1-900 nM and the reduction current was increased after each addition of NFT. The calibration plot establishes the relationship between the concentration of NFT and the reduction current with the ( $R^2$ ) as 0.9966 **(Fig.13(b))**. It confirms  $\text{GNR}/\text{MnO}_2/\text{GCE}$  makes an appropriate catalyst for the analysis of NFT. The lowest level of detection (LOD) is estimated as 0.3 nM.

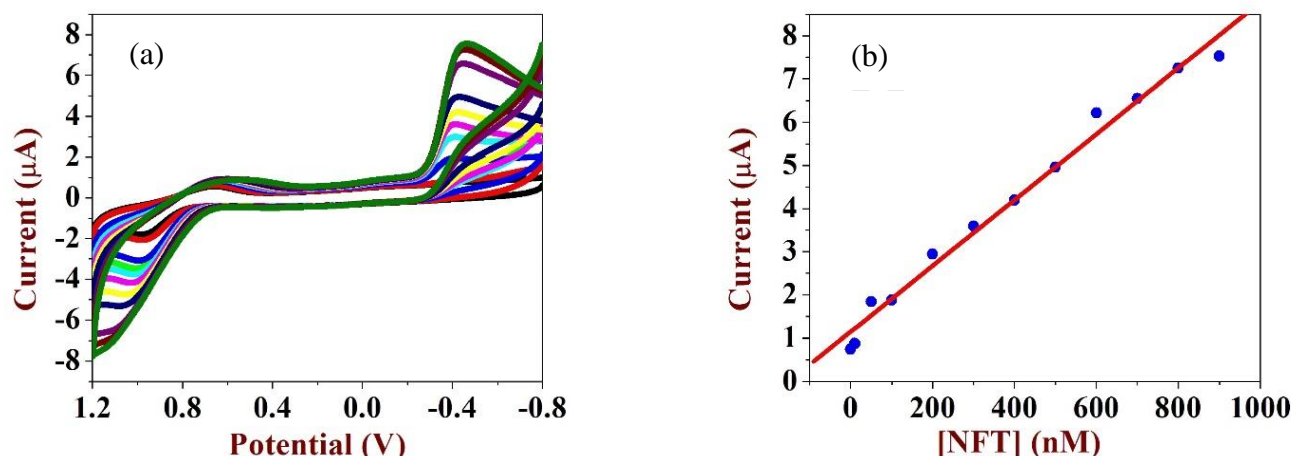


**Fig. 13.** (a) CVs for the concentration analysis of NFT in 0.1 phosphate buffer solution from 1-900 nM at the scan rate of 50 mV/s and (b) The relationship between the concentration of NFT vs. the reduction current ( $I_{pc}$ ).

The interference analysis was carried out with the NFT using the GNR/MnO<sub>2</sub>/GCE. The study was performed in the presence of various common molecules such as NA, NB, NP, SN, PN, L-isoleucine, and L-tyrosine which were added in the equal concentration of 100 nM with the analysis of 100 nM NFT (**Fig. 14**). The interfering molecules didn't show any significant changes towards the GNR/MnO<sub>2</sub>/GCE. Therefore, we concluded that GNR/MnO<sub>2</sub>/GCE has excellent selectivity performance towards the detection of NFT.

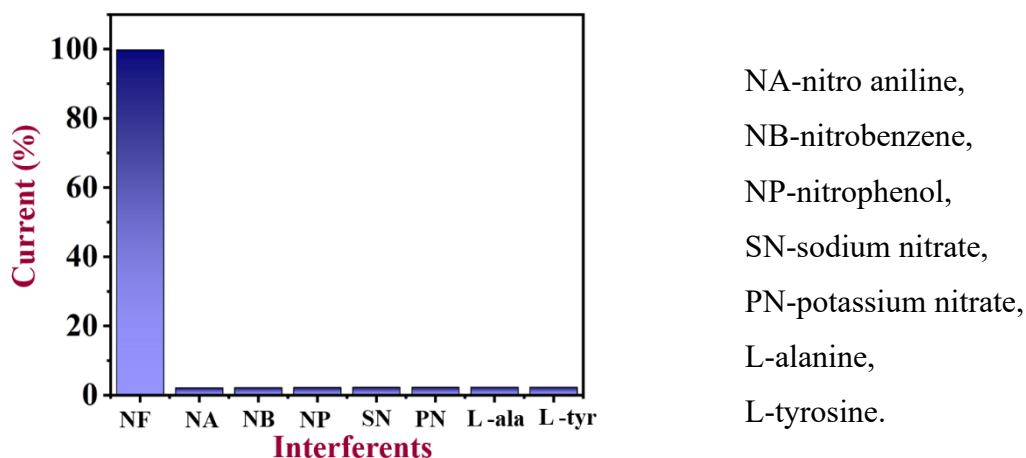


**Fig.14.** The interference analysis was done with the NFT using the GNR/MnO<sub>2</sub>/GCE.

# **CHAPTER 5**

## 5. CONCLUSION

In this work, the unzipping of MWCNTs was successfully demonstrated and the MnO<sub>2</sub> nanoplates were synthesized using hydrothermal methods. The modified GCE with GNR/MnO<sub>2</sub> nanocomposite was applied for the sensing of NFT with high sensitivity. The UV-Vis, XRD, HR-SEM and HR-TEM results showed the successful formation of MnO<sub>2</sub> nanoplates/GNR hybrid film. The analysis of NFT on the GNR/MnO<sub>2</sub> modified electrode shows the reduction peak at the potential of -0.38 V. In the concentration studies of NFT analysis, the linear range was estimated from 1-900 nM and the LOD was obtained as 0.3 nM. The selectivity has experimented with the several interfering molecules it confirms the GNR/MnO<sub>2</sub> modified electrode selectively towards NFT than the other interfernts. CV studies gave a wider linear range and lower detection limits which confirmed the GNR/MnO<sub>2</sub> is a promising sensor for NFT analysis.

# **CHAPTER 6**

## REFERENCE

- [1] J. Fraden, J. Fraden, Handbook of modern sensors: physics, designs, and applications, Springer, 2004.
- [2] A. Hulanicki, S. Glab, F. Ingman, Chemical sensors: definitions and classification, Pure Appl. Chem. 63 (1991) 1247–1250.
- [3] F. Mandoj, S. Nardis, C. Di Natale, R. Paolesse, Porphyrinoid thin films for chemical sensing, (2018).
- [4] W. Wen, Introductory chapter: What is chemical sensor?, IntechOpen, 2016.
- [5] T.R. Madhura, K.S.S. Devi, R. Ramaraj, Introduction to electrochemical sensors for the detection of toxic chemicals, in: Met. Oxides Nanocomposite-Based Electrochem. Sensors Toxic Chem., Elsevier, 2021: pp. 1–18.
- [6] Introduction To Electrochemical Sensors., (n.d.).  
<https://chem.libretexts.org/@go/page/283196>.
- [7] X. Xu, Intelligent composite materials for use as sensors and actuators, in: Compos. Mater., Elsevier, 2021: pp. 465–487.
- [8] F.R. Simões, M.G. Xavier, Electrochemical sensors, Nanosci. Its Appl. (2017) 155–178.
- [9] M.K.L. Coelho, J.D.F. Giarola, A.T.M. Da Silva, C.R.T. Tarley, K.B. Borges, A.C. Pereira, Development and application of electrochemical sensor based on molecularly imprinted polymer and carbon nanotubes for the determination of carvedilol, Chemosensors. 4 (2016) 22.
- [10] National Center for Biotechnology Information, PubChem Subst. Rec. (2022).  
<https://pubchem.ncbi.nlm.nih.gov/substance/24897842>.
- [11] J.D. Conklin, The pharmacokinetics of nitrofurantoin and its related bioavailability., Antibiot. Chemother. 25 (1978) 233–252.

- [12] K.-Y. Hwa, T.S.K. Sharma, Nano assembly of NiFe spheres anchored on f-MWCNT for electrocatalytic reduction and sensing of nitrofurantoin in biological samples, *Sci. Rep.* 10 (2020) 1–13.
- [13] R.A. Wijma, A. Huttner, B.C.P. Koch, J.W. Mouton, A.E. Muller, Review of the pharmacokinetic properties of nitrofurantoin and nitroxoline, *J. Antimicrob. Chemother.* 73 (2018) 2916–2926.
- [14] I. Stock, Nitrofurantoin--clinical relevance in uncomplicated urinary tract infections, *Med. Monatsschr. Pharm.* 37 (2014) 242–248.
- [15] L. Sánchez-Hernández, M.L. Marina, *Capillary Electrophoresis—Antibiotics*, (2016).
- [16] Y. Wang, T. Chen, Q. Zhuang, Y. Ni, Label-free photoluminescence assay for nitrofurantoin detection in lake water samples using adenosine-stabilized copper nanoclusters as nanoprobe, *Talanta*. 179 (2018) 409–413.
- [17] S. Birgisson, D. Saha, B.B. Iversen, Formation mechanisms of nanocrystalline MnO<sub>2</sub> polymorphs under hydrothermal conditions, *Cryst. Growth Des.* 18 (2018) 827–838.
- [18] C. Sun, Y. Zhang, S. Song, D. Xue, Tunnel-dependent supercapacitance of MnO<sub>2</sub>: effects of crystal structure, *J. Appl. Crystallogr.* 46 (2013) 1128–1135.
- [19] D. Wu, X. Xie, Y. Zhang, D. Zhang, W. Du, X. Zhang, B. Wang, MnO<sub>2</sub>/carbon composites for supercapacitor: synthesis and electrochemical performance, *Front. Mater.* (2020) 2.
- [20] J. Shin, J.K. Seo, R. Yaylian, A. Huang, Y.S. Meng, A review on mechanistic understanding of MnO<sub>2</sub> in aqueous electrolyte for electrical energy storage systems, *Int. Mater. Rev.* 65 (2020) 356–387.
- [21] J.E. Greedan, N.P. Raju, A.S. Wills, C. Morin, S.M. Shaw, J.N. Reimers, Structure and magnetism in  $\lambda$ -MnO<sub>2</sub>. Geometric frustration in a defect spinel, *Chem. Mater.* 10 (1998) 3058–3067.

- [22] Y. Wang, H. Guan, S. Du, Y. Wang, A facile hydrothermal synthesis of MnO<sub>2</sub> nanorod–reduced graphene oxide nanocomposites possessing excellent microwave absorption properties, *RSC Adv.* 5 (2015) 88979–88988.
- [23] X. Dong, Y. Zhang, Y. Xu, M. Zhang, Catalytic mechanism study on manganese oxide in the catalytic supercritical water oxidation of nitrobenzene, *Rsc Adv.* 5 (2015) 47488–47497.
- [24] L. Miao, J. Wang, P. Zhang, Review on manganese dioxide for catalytic oxidation of airborne formaldehyde, *Appl. Surf. Sci.* 466 (2019) 441–453.
- [25] H. Wang, H.S. Wang, C. Ma, L. Chen, C. Jiang, C. Chen, X. Xie, A.-P. Li, X. Wang, Graphene nanoribbons for quantum electronics, *Nat. Rev. Phys.* 3 (2021) 791–802.
- [26] P. Shende, S. Augustine, B. Prabhakar, A review on graphene nanoribbons for advanced biomedical applications, *Carbon Lett.* 30 (2020) 465–475.
- [27] C. Bronner, Bottom-Up Synthesis and Electronic Structure of Graphene Nanoribbons on Surfaces, (2018).
- [28] A. Celis, M.N. Nair, A. Taleb-Ibrahimi, E.H. Conrad, C. Berger, W.A. De Heer, A. Tejeda, Graphene nanoribbons: fabrication, properties and devices, *J. Phys. D: Appl. Phys.* 49 (2016) 143001.
- [29] E. Mehmeti, D.M. Stanković, A. Hajrizi, K. Kalcher, The use of graphene nanoribbons as efficient electrochemical sensing material for nitrite determination, *Talanta.* 159 (2016) 34–39.
- [30] Q. Liu, K. Jiang, J. Fan, Y. Lin, Y. Min, Q. Xu, W.-B. Cai, Manganese dioxide coated graphene nanoribbons supported palladium nanoparticles as an efficient catalyst for ethanol electrooxidation in alkaline media, *Electrochim. Acta.* 203 (2016) 91–98.
- [31] B. He, J. Li, A sensitive electrochemical sensor based on reduced graphene oxide/Fe<sub>3</sub>O<sub>4</sub> nanorod composites for detection of nitrofurantoin and its metabolite, *Anal. Methods.* 11 (2019) 1427–1435.



- [32] S.V. Selvi, R. Rajakumaran, S.-M. Chen, A.M. Rady, S. Veerasankar, T.-W. Chen, S.-P. Rwei, B.-S. Lou, Graphene/Tungsten trioxide (Gr/WO<sub>3</sub>) composite modified screen-printed carbon electrode for the sensitive electrochemical detection of nitrofurantoin in biological samples, *Int. J. Electrochem. Sci.* 14 (2019) 6454–6467.
- [33] Z.-L. Wu, C.-K. Li, J.-G. Yu, X.-Q. Chen, MnO<sub>2</sub>/reduced graphene oxide nanoribbons: facile hydrothermal preparation and their application in amperometric detection of hydrogen peroxide, *Sensors Actuators B Chem.* 239 (2017) 544–552.
- [34] A.V. Rane, K. Kanny, V.K. Abitha, S. Thomas, Methods for synthesis of nanoparticles and fabrication of nanocomposites, in: *Synth. Inorg. Nanomater.*, Elsevier, 2018: pp. 121–139.
- [35] M.D. Shete, J.B. Fernandes, A simple one step solid state synthesis of nanocrystalline ferromagnetic  $\alpha$ -Fe<sub>2</sub>O<sub>3</sub> with high surface area and catalytic activity, *Mater. Chem. Phys.* 165 (2015) 113–118.
- [36] E. Suvacı, E. Özel, Hydrothermal synthesis, *Encycl. Mater. Tech. Ceram. Glas.* (2021).
- [37] G. Huang, C.-H. Lu, H.-H. Yang, Magnetic nanomaterials for magnetic bioanalysis, in: *Nov. Nanomater. Biomed. Environ. Energy Appl.*, Elsevier, 2019: pp. 89–109.
- [38] O. Sadak, W. Wang, J. Guan, A.K. Sundramoorthy, S. Gunasekaran, MnO<sub>2</sub> nanoflowers deposited on graphene paper as electrode materials for supercapacitors, *ACS Appl. Nano Mater.* 2 (2019) 4386–4394.